

PAPER • OPEN ACCESS

Microstructure, pinning properties, and aging of CSD-grown $\text{SmBa}_2\text{Cu}_3\text{O}_{7-\delta}$ films with and without BaHfO_3 nanoparticles

To cite this article: Jens Hänisch *et al* 2022 *Supercond. Sci. Technol.* **35** 084009

View the [article online](#) for updates and enhancements.

You may also like

- [Characteristics of high-performance \$\text{BaHfO}_3\$ -doped \$\text{SmBa}_2\text{Cu}_3\text{O}_7\$ superconducting films fabricated with a seed layer and low-temperature growth](#)
S Miura, Y Yoshida, Y Ichino *et al.*
- [Flux pinning landscape up to 25 T in \$\text{SmBa}_2\text{Cu}_3\text{O}_7\$ films with \$\text{BaHfO}_3\$ nanorods fabricated by low-temperature growth technique](#)
Yuji Tsuchiya, Shun Miura, Satoshi Awaji *et al.*
- [Epitaxial \$\text{YBa}_2\text{Cu}_3\text{O}_{7-x}\$ nanocomposite films and coated conductors from \$\text{BaMO}_3\$ \(\$M = \text{Zr, Hf}\$ \) colloidal solutions](#)
X Obradors, T Puig, Z Li *et al.*













IOP | ebooks™

Bringing together innovative digital publishing with leading authors from the global scientific community.

Start exploring the collection—download the first chapter of every title for free.

Microstructure, pinning properties, and aging of CSD-grown $\text{SmBa}_2\text{Cu}_3\text{O}_{7-\delta}$ films with and without BaHfO_3 nanoparticles

Jens Hänisch^{1,*} , Kazumasa Iida^{2,3} , Pablo Cayado^{4,*} , Manuela Erbe¹ ,
Lukas Grünewald⁵ , Takafumi Hatano² , Tatsunori Okada⁶ , Dagmar Gerthsen⁵ ,
Satoshi Awaji⁶  and Bernhard Holzapfel¹ 

¹ Institute for Technical Physics, Karlsruhe Institute of Technology, Hermann-von-Helmholtz-Platz 1, Eggenstein-Leopoldshafen, 76344, Germany

² Department of Materials Physics, Nagoya University, Furo-cho, Chikusa-ku, Nagoya 464-8603, Japan

³ Department of Electrical and Electronic Engineering, College of Industrial Technology, Nihon University, 1-2-1 Izumi-cho, Narashino-shi, Chiba 275-8575, Japan

⁴ Department of Quantum Matter Physics (DQMP), University of Geneva, Quai Ernest-Ansermet 24, 1211 Geneva, Switzerland

⁵ Karlsruhe Institute of Technology, Laboratory for Electron Microscopy, 76131 Karlsruhe, Germany

⁶ High Field Laboratory for Superconducting Materials, Institute for Materials Research, Tohoku University, Katahira 2-1-1, Aoba-ku, Sendai 980-8577, Japan

E-mail: jens.haenisch@kit.edu and Pablo.Cayado@unige.ch

Received 6 April 2022, revised 1 June 2022

Accepted for publication 22 June 2022

Published 6 July 2022



CrossMark

Abstract

In order to improve the electrical transport properties of $\text{REBa}_2\text{Cu}_3\text{O}_{7-\delta}$ nanocomposite films, $\text{SmBa}_2\text{Cu}_3\text{O}_{7-\delta}$ films with and without BaHfO_3 nanoparticles were grown by chemical solution deposition, and their microstructural and transport properties were investigated in a detailed study using transmission electron microscopy and transport measurements in magnetic fields up to 24 T. The optimization process of the crystallization step (temperature and oxygen partial pressure) as well as an aging effect, which is due to the release of trapped fluorine, are described. Critical temperature and critical current densities surprisingly improve initially during the aging. Due to the complex microstructure, the additional BaHfO_3 nanoparticles have only a positive effect at low magnetic fields for our samples.

Supplementary material for this article is available [online](#)

Keywords: SmBCO, CSD, BHO, J_c , flux pinning, TEM

(Some figures may appear in colour only in the online journal)

* Authors to whom any correspondence should be addressed.



1. Introduction

Due to their exceptional performance not only at liquid-nitrogen temperature but also in high magnetic fields at low temperatures or medium field and temperature ranges, $REBa_2Cu_3O_{7-\delta}$ (*RE*: rare earth, *REBCO*) phases are the compounds of choice for advanced high-temperature superconducting wires and tapes. These are the so-called coated conductors, where the functional material *REBCO* is deposited epitaxially on long metallic tapes with certain buffer layer architectures [1, 2].

One of the *REBCO* compounds that gained interest in recent years is $Sm_{1+x}Ba_{2-x}Cu_3O_{7-\delta}$ with superconducting transition temperature (T_c) as high as 95 K [3]. Due to the relatively large ion size of Sm^{3+} , it is prone to Sm–Ba disorder and off-stoichiometries degrading T_c and the transport properties. Therefore, the phase formation is somewhat challenging, yet not as severe as for LaBCO or NdBCO. Nevertheless, SmBCO films have been successfully prepared not only by pulsed laser deposition (PLD) [4, 5], but also by metalorganic chemical vapour deposition (MOCVD) [6], laser CVD [7], sputtering [8], co-evaporation [9], liquid-phase epitaxy [10], and chemical solution deposition (CSD). The latter has not only been shown in the usual trifluoroacetate metalorganic decomposition (TFA-MOD) [11, 12], but also with extremely-low-fluorine [13] and fluorine-free solutions [14]. In fact, SmBCO has already been used as functional material for coated conductor research and production [15, 16].

In order to improve and optimize the current carrying capabilities of *REBCO* films and coated conductors for a certain application with a specific range in temperature and magnetic field, artificial pinning centres have to be introduced [2]. Besides mixing *RE* elements [17], transition metal doping [11], adjusting the stacking fault (SF) density [18] (here YBCO), multilayering and adjusting the Sm–Ba ratio [19], surface decoration [20], and irradiation [21], the best-investigated method is probably the insertion of non-superconducting nanoparticles (for reviews see [22–24]), such as perovskites or occasionally pyrochlores [25]. For SmBCO, the former has been intensively investigated by Yoshida *et al* on PLD-grown films [26]. Due to the columnar growth mode during PLD, perovskites usually self-organize in more or less *c*-axis-oriented nanocolumns [27], leading to huge *c*-axis peaks in the angular dependence of the critical current density J_c [26], distinct matching effects [28] as well as a usual slight T_c decrease [29].

For CSD-grown films, the addition of perovskite nanoparticles has mainly been investigated for YBCO, e.g. [30–32], as well as GdBCO [30, 33] and (Gd,Y)BCO, e.g. [34, 35]. Recently, we started to systematically extend these investigations to other *REBCO* compounds [12]. According to this study, the most suitable substrate and the optimum deposition conditions depend on both the *RE* and the presence of the perovskite, here $BaHfO_3$ (BHO), often also $BaZrO_3$ (BZO).

Here, we investigate the influence of BHO nanoparticles on microstructure and current carrying capability of optimized SmBCO films grown by full-TFA MOD, which has not been studied before.

2. Experimental

2.1. Sample preparation

The TFA-MOD precursor solutions were prepared following the recipe of [12, 36]: the acetates of Sm, Ba, and Cu (>99.99%, *Alfa Aesar*) of ratio 1:2:3 were dissolved in water, mixed with surplus of trifluoroacetic acid (99.5+%, *Alfa Aesar*), and stirred until complete dissolution of the metalorganic salts at room temperature. These solutions were concentrated with a rotary evaporator, re-diluted in ultra-dry methanol (>99.9%, $H_2O < 50$ ppm, *Carl Roth*) and filled up to the final concentration of the *RE* of 0.25 mol l^{-1} . For the nanocomposite solutions, hafnium(IV)-2,4-pentanedionate ($Hf(acac)_4$, 97+%, *Alfa Aesar*) and an according molar amount of barium acetate, dissolved in water, were added to the solutions for nominally 12 mol% of BHO in the films. For BZO as nanoparticles, it had been reported that the amount should be limited to 10 mol% in order to avoid nanoparticle coarsening [37, 38]. For BHO, our earlier (unpublished) experiments with several *REBCO* phases suggest a quite similar amount of 12 mol% as optimum because the coarsening is still not excessive but the pinning improvement considerable. Afterwards, minute amounts of acetylacetone (0.6 $acac/RE$ ion or 1.5 vol% in final solution) were added to protect them from impurities such as water. The solutions were then filtered through polytetrafluoroethylene with $0.2 \mu\text{m}$ pore size and spin-coated with 6000 rpm for 30 s on cleaned $10 \text{ mm} \times 10 \text{ mm}$ (001)-oriented single crystals of $LaAlO_3$ (LAO) resulting in a film thickness of around 220 nm. The films were heat-treated (for details see [36]) with a crystallization oxygen partial pressure p_{O_2} of 50 or 150 ppm in nitrogen at 1 atm total pressure (dew point $T_{\text{dew}} = 19 \text{ }^\circ\text{C}$) and crystallization temperatures between $780 \text{ }^\circ\text{C}$ and $860 \text{ }^\circ\text{C}$. Afterwards, the sample cooled down in dry nitrogen with the same p_{O_2} and gas flux as used during the film growth to $450 \text{ }^\circ\text{C}$ for the final oxygenation in 1 bar oxygen.

2.2. Structural characterization

Structural features of the films were measured by x-ray diffraction (XRD; D8 Discover, *Bruker*, Cu- $K\alpha$ radiation) and scanning electron microscopy (SH-5000P, *Hirox*, tungsten cathode, SE-detector, 10 kV acceleration voltage). Layer thickness and surface topography were determined by atomic force microscopy (Dimension Edge, *Bruker*) in tapping mode on bridges used for electrical transport measurements, and occasionally cross-checked by transmission electron microscope (TEM).

Cross-section samples for scanning TEM (STEM) were prepared by an *in-situ* lift-out technique [39] in a FEI Strata 400S focused-ion beam (FIB)/scanning electron microscope system. High- and low-angle annular dark-field (HAADF/LAADF)-STEM images were taken with a FEI Titan³ 80–300 TEM operated at 300 kV. The HAADF-STEM image intensity is sensitive to the average atomic number Z , where a larger Z results in higher HAADF-STEM intensity for a sample with reasonably constant TEM-sample thickness. In contrast, LAADF-STEM images also show diffraction

contrast and reveal more clearly crystalline defects and lattice strain. Chemical analysis with energy-dispersive x-ray spectroscopy (EDXS) was carried out with a FEI Tecnai Osiris microscope operated at 200 kV with ChemiSTEM technology [40]. The EDXS mapping data set was denoised with principal component analysis [41] before extracting the elemental signals with a peak-fitting routine using the HyperSpy Python-package [42, 43].

2.3. Electromagnetic measurements

The films were scanned for their superconducting properties by inductive techniques: the transition temperature T_c (defined as 10%, 50% and 90% of the normal-state value) by a self-made mutual-inductance device, and the self-field critical current density at 77 K in a Cryoscan (*THEVA*, 50 μV criterion). The ~ 50 μm wide and 1 mm long bridge structures for 4-point transport measurements on selected samples were photolithographically prepared with an image-reversal photoresist (AZ5214E, *Microchemicals*) plus wet-chemical etching in an aqueous 0.6 wt% HNO_3 solution. For lowering the contact resistances, Au pads were prepared by PLD. The electrical contacts were provided by Cu wires attached with silver paint.

Field, temperature, and orientation dependence of J_c in magnetic fields up to 14 T were determined via the measurement of voltage–current (V – I) characteristics in a Physical Properties Measurement System (Quantum Design) with rotator stage and a self-made LabVIEW measurement software controlling a Nanovoltmeter 2182 A and a SourceMeter 2460 by Keithley. J_c was determined with an electrical field criterion E_c of 1 $\mu\text{V cm}^{-1}$. The N value ($V \sim I^N$) was determined by fits of $\log(V)$ vs $\log(I)$ in 1–2 decades above E_c .

The upper critical field B_{c2} and the irreversibility field B_{irr} were determined via temperature dependent resistivity measurements, $\rho(T)$, at constant applied fields $B \parallel c$ and a bias current of 100 μA . The criteria were 75% of normal state resistivity above T_c and $\rho_{irr} = E_c/100 \text{ A cm}^{-2}$, respectively. T_c and T_{irr} , i.e. zero-resistivity T_c , were determined accordingly. For evaluating B_{c2} additionally, extrapolation to zero of the logarithmic derivative $(d \ln R/dT)^{-1}$ was used in order to be more criterion-independent, figure S1. The activation energy U_0 of thermally activated flux motion was determined by linear fits of the Arrhenius plots $\ln(R)$ vs. $1/T$ in the region of highest linearity.

The two top-performing samples of the pristine and the nanocomposite series were analysed further in d.c. fields up to 24 T in the 25 T cryogen-free superconducting magnet at IMR Tohoku University. For measuring the angular dependence of J_c , the magnetic field B was applied in maximum Lorentz force configuration at different angles θ measured from the c -axis.

3. Microstructural properties

The optimized films with respect to their superconducting properties show a rather smooth and dense surface morphology, figure 1, with occasional pinholes (left image) and superficial grooves in nanocomposite films (right image). The

pristine samples are in general slightly smoother, yet contain some amount of needle-like a -axis oriented grains. Lower crystallization temperatures (<800 $^\circ\text{C}$) lead to an increased density and size of these a -axis grains and other needle-like outgrowths, especially for the nanocomposites and/or 150 ppm O_2 . An increase of a -axis grains with oxygen partial pressure in TFA-MOD SmBCO films was also found by Mitani *et al* [44]. At higher crystallization temperatures (>830 $^\circ\text{C}$), round precipitates of ~ 1 μm diameter (most likely CuO) are visible for the pristine films, especially at 50 ppm O_2 . The nanocomposites do not show these precipitates but occasionally contain very large foreign phases of ~ 10 μm at even higher temperature (>840 $^\circ\text{C}$).

The XRD θ – 2θ scans, figure 2, show the expected pattern of c -axis-oriented films with only *REBCO*(00 l) reflections besides reflections of the substrate and occasional foreign phases. The above-mentioned a -axis grains (*cf* the 200 reflection of SmBCO) are visible for the as-grown films next to the SmBCO 006 peak. Re-measuring the samples 1.5 years after deposition reveals an interesting aging effect by the appearance of extra peaks mainly between 20° and 40° , especially CuO, $\text{Sm}_2\text{Cu}_2\text{O}_5$, and F-containing phases of the system BaF_2 – SmF_3 [45]. This is surprising. Apparently, the fluorine is not fully taken out of the film during our growth process and is either trapped in small voids as OF phase [46] (peak at 24.9° for the as-deposited films) or presumably even partly entering the SmBCO crystal structure forming $\text{Sm}_{1+y}\text{Ba}_{2-x}\text{Cu}_3\text{F}_{2y}\text{O}_{6.5-y+\delta}$ as described in literature for the YBCO pendant [47, 48], which may release the fluorine over time. This released fluorine reacts with Sm and Ba species which leads to the appearance of other foreign phases for stoichiometric reasons. Due to possible strain and composition variations, a final identification of all phases is not possible from XRD alone. Also, neither $\text{Sm}_2\text{Cu}_2\text{O}_5$ nor the Ba–Sm–F phases are available in the Inorganic Crystal Structure Database (ICSD). However, both have been extensively described for the Y case, e.g. [49], and were here inferred from $\text{Y}_2\text{Cu}_2\text{O}_5$ and Ba–Y–F, respectively. Smith *et al* recently mentioned the possibility of the $\text{RE}_2\text{Cu}_2\text{O}_5$ phase for GdBCO coated conductors [50], although its stability is assumed to decrease with increasing RE ion radius and had not been reported for larger lanthanoids than Tb [51]. Noteworthy, $\text{Y}_2\text{Cu}_2\text{O}_5$ has been tried as artificial pinning centres recently in bulk YBCO samples, although with considerable T_c reduction [52]. Nevertheless, also BaCuO_2 (which is in equilibrium with *REBCO* and $\text{RE}_2\text{Cu}_2\text{O}_5$ at high temperatures [53]) has been described by Park *et al* [54] as a peak triplet around 30° for GdBCO coated conductors fabricated by reactive co-evaporation. Wang *et al* [55] show Sm_2CuO_4 and CuO in MOCVD-grown SmBCO films with peaks near 30° , and Naik *et al* [56] identify a peak near 36° with CuO for infiltration-grown YBCO bulk samples. This aging leads to an increase in T_c by ~ 0.5 K and of the self-field J_c by a factor of up to 1.5 within 2 years (supplement S2) even though the intensity of the SmBCO peaks is decreasing. The newly developed foreign phases most likely contribute to the flux pinning.

The microstructure of one of the nanocomposite films (150 ppm, 830 $^\circ\text{C}$) was investigated in more detail by STEM.

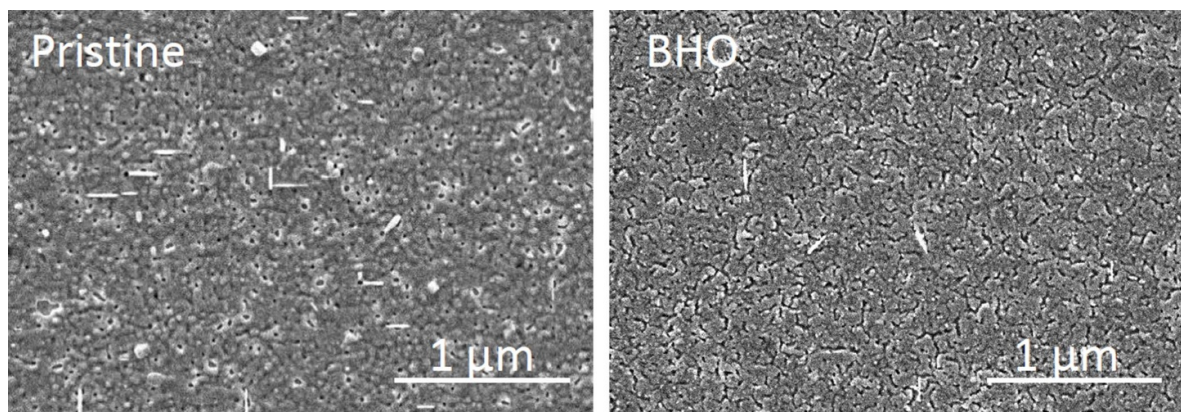


Figure 1. Surface morphology of a pristine (left) and a BHO nanocomposite SmBCO film (right) prepared under optimized conditions (50 ppm; 820 °C and 810 °C respectively). The needle shaped grains with bright contrast (left) are *a*-axis-oriented SmBCO grains.

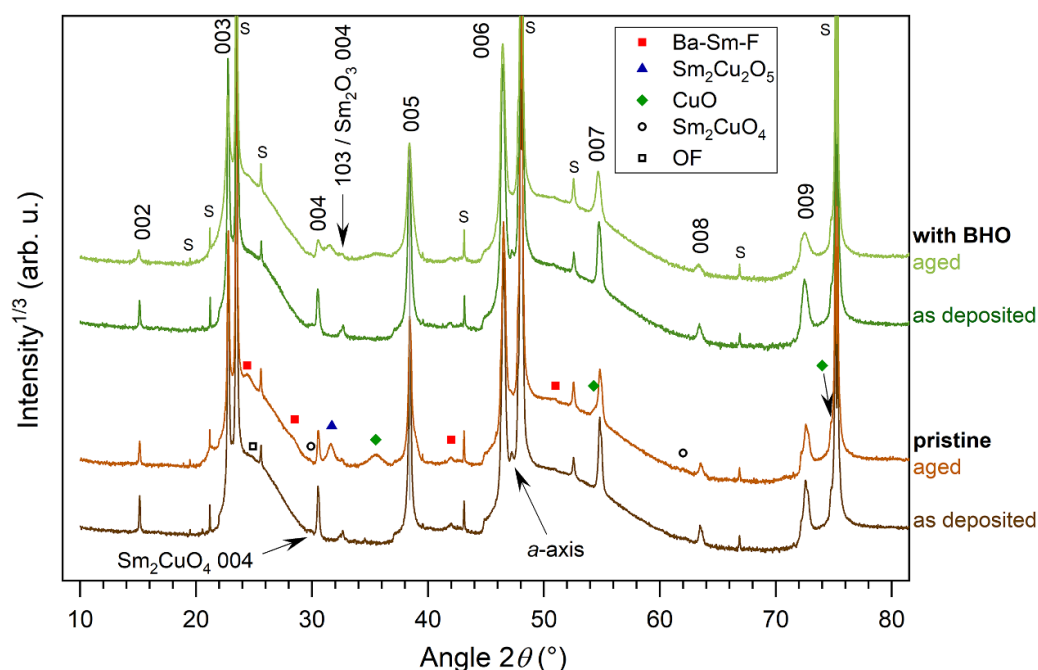


Figure 2. XRD θ - 2θ scans of a pristine and a BHO nanocomposite SmBCO film, both shortly after growth and 1.5 years later. S: substrate or setup-related peaks.

The elemental maps obtained by STEM-EDXS (figure 3) show a homogeneous spatial distribution of the BHO nanoparticles (see Hf and combined Ba/Hf/Sm distributions in figure 3). A few Sm-rich and Ba-depleted precipitates are visible at the substrate-film interface (marked by arrows). One of these precipitates was identified to consist of the Sm_2CuO_4 phase as shown below.

The LAADF-STEM overview image of the film in figure 4(a) shows a region with BHO nanoparticles at the surface, in the film, and at the film/substrate interface marked by red, green, and blue lines, respectively. The film has a thickness of about 260 nm. However, a thinner region (marked by dotted white lines) is observed, where BHO particles are absent in the film but seem to float on the surface. Such a thin region was only observed once in the investigated TEM sample. An average equivalent diameter μ_a of 20.5 nm with a

standard deviation σ of 7.3 nm (figure 4(d)) was determined from all BHO nanoparticles in figure 4(a). A Sm-rich precipitate at the film/substrate interface with slightly increased intensity compared to the film is visible at higher magnification (figure 4(c)). Extended SFs, i.e. extra CuO planes, appear as dark horizontal lines (marked by yellow dashed arrows in figure 4(b)) at higher magnification. A particularly high SF density is found in the vicinity of the film/substrate interface, near BHO particles, and close to the surface, which was also observed for other REBCO films [12]. In addition, short SFs of only a few nm in length are distributed throughout the film (e.g. in the region marked by a dashed circle in figure 4(b)), which cause a local buckling of the surrounding SmBCO unit cells. We suspect that the short SFs in the shown TEM samples were induced during TEM-sample preparation as suggested by Zhu *et al* [57] or by TEM-sample degradation

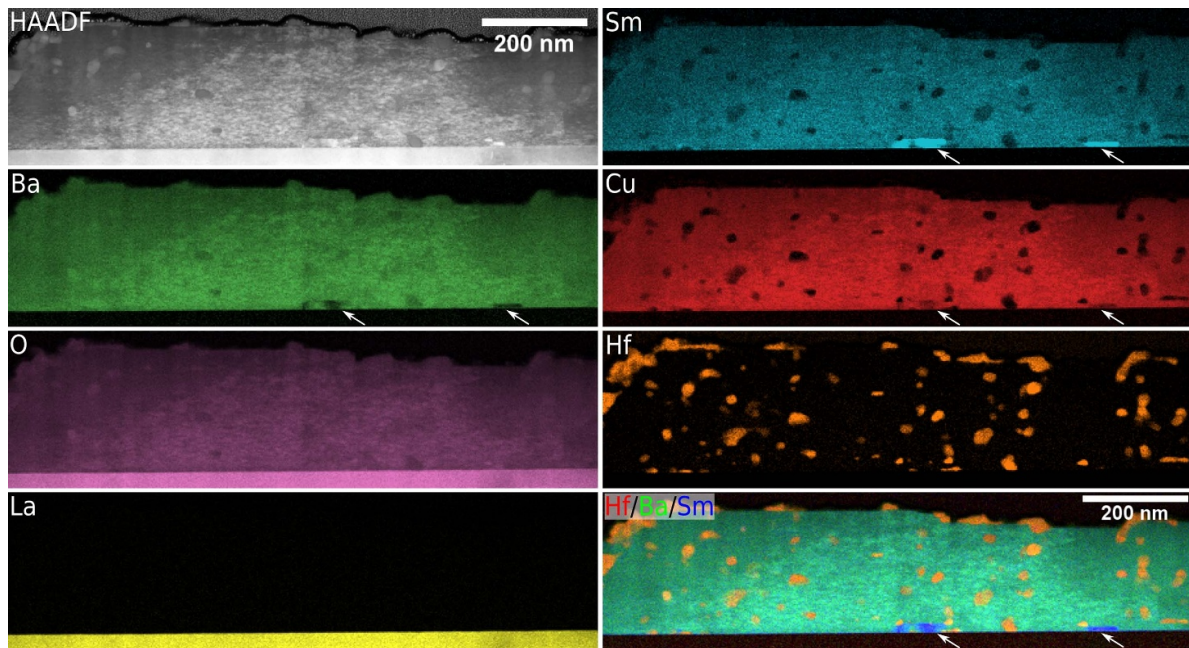


Figure 3. Qualitative elemental maps of SmBCO with 12 mol% BHO obtained by STEM-EDXS analysis. The arrows in the Sm, Ba, Cu maps, and the Hf–Ba–Sm composite map mark Sm-rich precipitates (possibly Sm_2CuO_4) at the film/substrate interface. A homogeneous distribution of BHO nanoparticles is visible as demonstrated by the Hf map. Spurious Cu x-rays from the used Cu TEM grid cause an additional Cu signal.

in air [58, 59]. The TEM samples in this work were investigated after FIB preparation and exposure to ambient air of about 20 min during transfer between the FIB and TEM instruments. At the film/substrate interface, bright structures are visible in LAADF-STEM images (*cf* black arrows in figure 4(b)) which are most likely induced by strain fields [60] from steps at the film/substrate interface or dislocations.

High-resolution HAADF-STEM imaging of the film near the interface reveals an in-plane shift by $a/2$ (or $b/2$) for the first unit cell of SmBCO (inset in figure 5(a)), whereas cube-on-cube growth without such an in-plane shift was also reported for REBCO growth on LAO [57]. The HAADF-STEM image also shows the aforementioned high density of short SFs in the film (examples marked by circles in figure 5(a)). Epitaxial growth with the crystallographic relationship $(001)[100]\text{SmBCO} \parallel (001)[100]\text{LAO}$ is confirmed by Fourier-transform analysis of the film/substrate interface region (*cf* figure 5(b) and supplementary information figures S3(a) and (b)). According to the high-resolution HAADF-STEM image figure 5(a), the SmBCO film grows slightly tilted around the beam/viewing direction (about 1°) on the LAO substrate, presumably due to the growth on a vicinal LAO surface with periodic substrate steps.

A Sm-rich precipitate in the HAADF-STEM image in figure 5(c) was identified as Sm_2CuO_4 (ICSD code 71182 [61]) based on Fourier-transform analysis of the red-dashed region in figure 5(c) (*cf* supplementary information figures S3(c) and (d)). Only a small lattice parameter mismatch exists between the $\text{Sm}_2\text{CuO}_4(020)$ and $\text{LAO}(020)$ planes as demonstrated by the overlaid power spectra from the Sm_2CuO_4 and LAO regions (*cf* red/blue reflections in figure 5(d) and supplementary information figures S3(c) and (d)).

The Sm_2CuO_4 phase is consistent with the STEM-EDXS results since a reduction of the Cu signal is observed for Sm_2CuO_4 (*cf* arrows in the Cu map of figure 3). The observed Cu depletion in Sm_2CuO_4 (nominal composition of 29 at.% Sm, 14 at.% Cu, and 57 at.% O) with respect to $\text{SmBa}_2\text{Cu}_3\text{O}_7$ matrix (nominal composition of 8 at.% Sm, 15 at.% Ba, 23 at.% Cu, and 54 at.% O) agrees with the chemical compositions of both phases. Note that the Cu $L\alpha$ x-ray transition was used here to extract the elemental map of Cu, which is less affected by spurious Cu x-rays than the Cu $K\alpha$ x-ray transition. The high-energy Cu $K\alpha$ x-rays (~ 8.05 keV) can more easily escape and penetrate the Cu TEM grid, whereas the low-energy Cu $L\alpha$ x-rays (0.93 keV) mainly originate from the TEM sample.

4. Electrical transport properties

4.1. Sample optimization

From experience, we regarded the crystallization temperature T_{crys} and the oxygen partial pressure p_{O_2} during crystallization as the most significant parameters. Consequently, while keeping the water vapour, i.e. the dew point T_{dew} constant at 19°C , we varied T_{crys} at two oxygen partial pressures, which were promising from former studies [12] taking into account that the optimum partial pressure decreases with increasing RE ion size [17, 62]. The lower oxygen partial pressure of 50 ppm yielded higher critical temperatures and self-field critical current densities compared to 150 ppm, figure 6. The optimum crystallization temperature, especially with respect to J_c , lies at $820 \pm 10^\circ\text{C}$ for nanocomposites at both partial pressures as well as the pristine films at 150 ppm, whereas 50 ppm

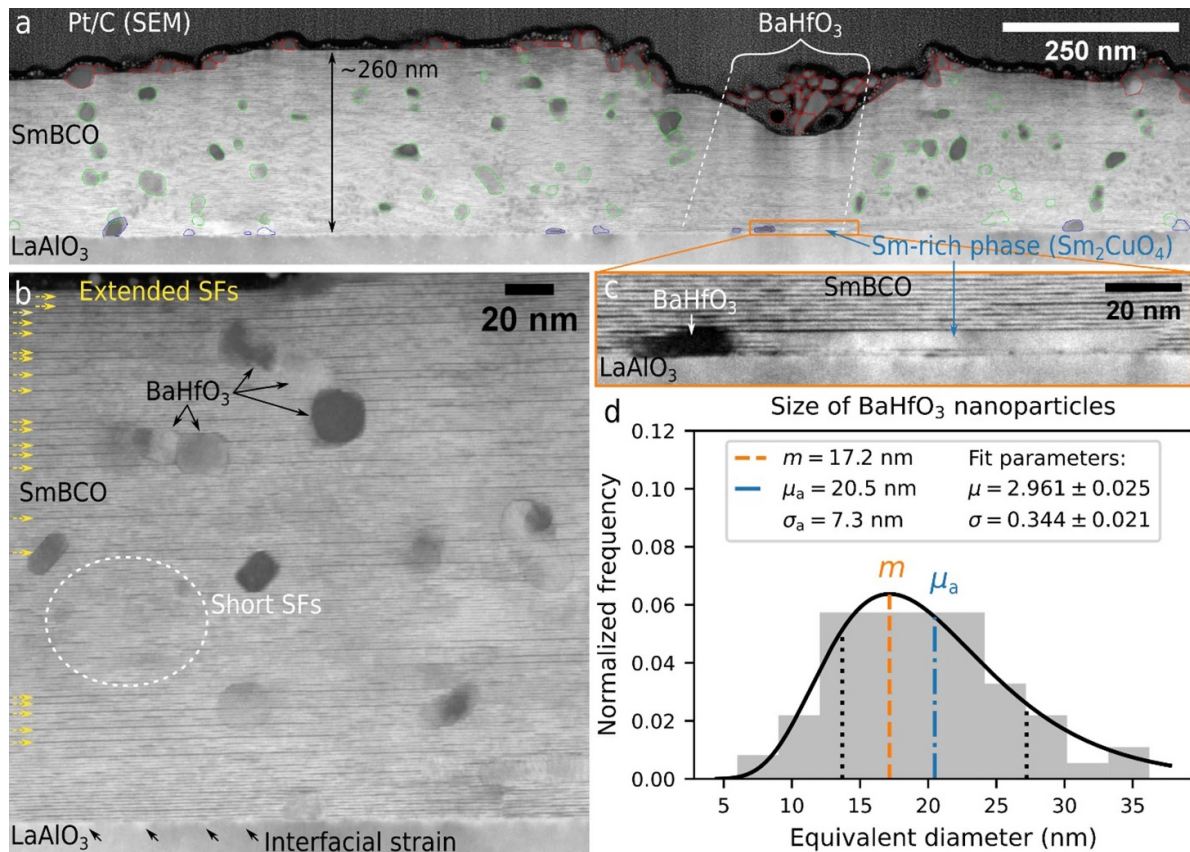


Figure 4. LAADF-STEM cross-section images of a SmBCO film with 12 mol% BHO on a LAO substrate. (a) LAADF-STEM overview image showing the microstructure and distribution of BHO nanoparticles at the interface (blue), in the film (green), and at the surface (red). In the thinnest region, BHO particles are not embedded in the film but instead agglomerated on the surface (marked by a bracket and the dashed white lines). An epitaxially aligned Sm-rich precipitate is found at the interface, which is identified as Sm_2CuO_4 (see also figure 5(c)). (b) Higher-magnification LAADF-STEM image showing BHO nanoparticles, extended SFs (yellow arrows), short SFs (e.g. in the circled region), and interface strain (black arrows) visualized by LAADF-diffraction contrast. (c) Magnified image of the interface from (a), which shows a dark BHO particle and a Sm-rich particle with high intensity. (d) Histogram of calculated area-equivalent diameters for the 121 BHO nanoparticles marked in (a) and fitted log-normal distribution (solid black line). The vertical lines show the position of the maximum (or mode) m (dashed orange line) and arithmetic mean μ_a (dashed-dotted blue line). The interval indicated by dotted lines contains 68.3% of the total area under the curve.

O_2 allows even lower $T_{\text{crys}} < 800$ °C for the pristine films. Crystallization temperatures below 780 °C were not reasonable anymore because of increasing porosity and formation of misorientations. Also for lower oxygen partial pressures, the system seems to be not stable anymore. For extreme-low-fluorine CSD-grown SmBCO films for example, 20 ppm yielded lower J_c values than 50 ppm [13].

In this optimized parameter range, the resistive transition width, the zero-resistivity T_c value, and the temperature dependence of the irreversibility field B_{irr} are very similar, except for the highest T_{crys} values at 50 ppm and the nanocomposites at 150 ppm, which show lower irreversibility lines $B_{\text{irr}}(T)$, figure 7.

The pinning force densities $F_p(B)$, measured 1.5 years after deposition, show some variability for the optimized parameter range, see figure 8 for the 65 K data as an example. Where the pristine samples have a maximum pinning force density $F_{p\text{max}}$ of 10 ± 2 GN m^{-3} , the nanocomposites show slightly better values of 14 ± 3 GN m^{-3} . This trend is also visible for other measurement temperatures. This increase due to the

BHO nanoparticles of $\sim 30\%$ (best samples) compares well with earlier results on GdBCO + BHO [30], however are well below values for recent GdBCO, as well as GdYBCO, and YBCO systems, see table 1. So, the achievable increase in $F_{p\text{max}}$ due to randomly oriented nanoparticles seems to depend in part also on RE ion size (most likely via the respective microstructures) besides nanoparticle size [34] and content. However, one has to take into account the much larger advance and data availability for the other systems.

4.2. Resistive transition, activation energy and phase diagram

The resistive transitions of pristine and BHO-added SmBCO films are remarkably similar, figure 9. Both kinds of samples, if optimized, show a very small zero-field transition width of ~ 1 K and comparable normal state resistances of 120 Ω at 100 K (i.e. ~ 130 $\mu\Omega$ cm). Via the Arrhenius plots of these data, the activation energy $U_0 = -d\ln R/d(kT)^{-1}$ of thermally activated flux motion was determined, figure 10. The

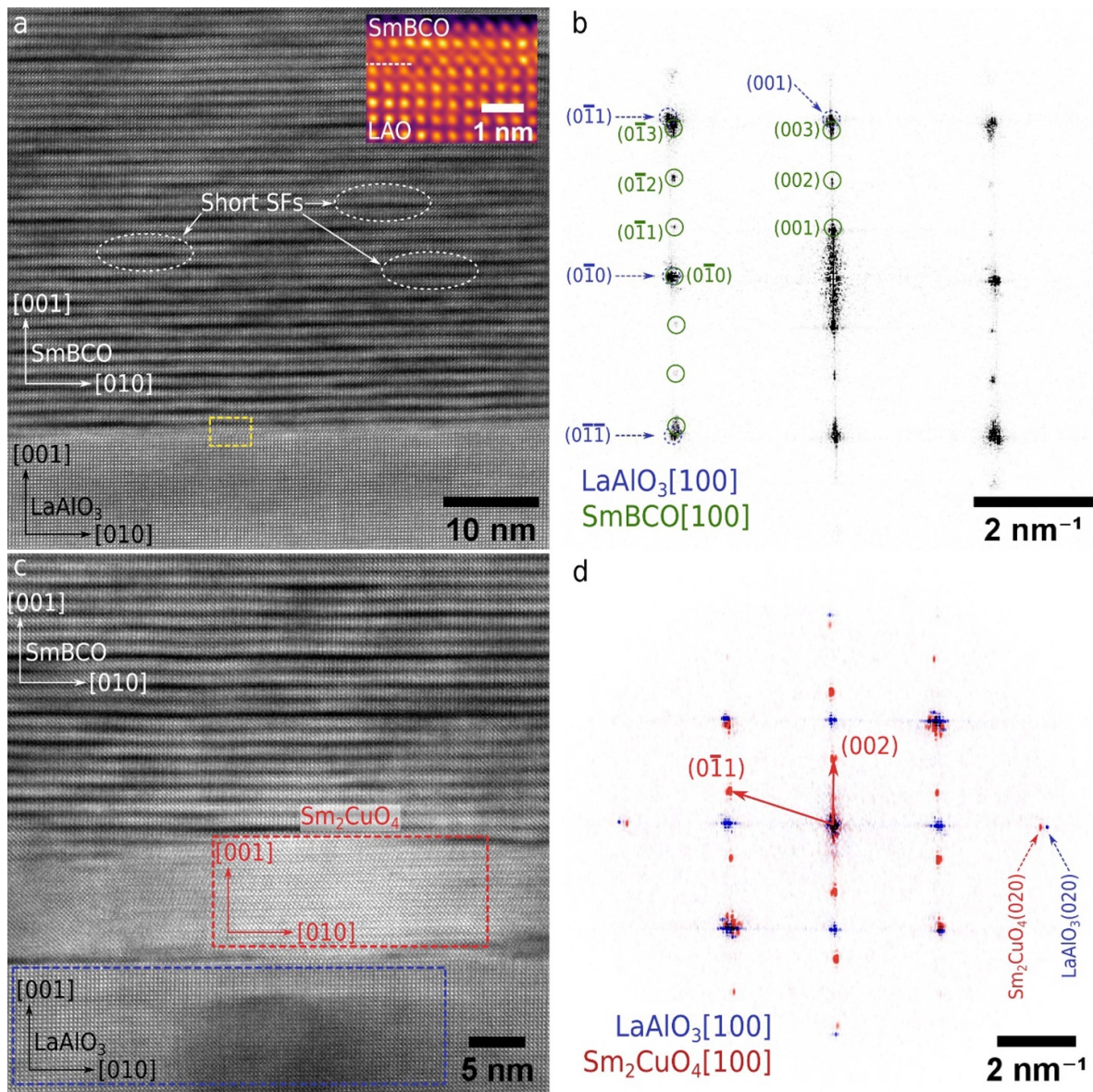


Figure 5. (a) High-resolution HAADF-STEM image and (b) corresponding power spectrum of the film/substrate interface region showing epitaxial growth of (001)[100]SmBCO|| (001)[100]LAO (*cf* also supplementary information figures S3(a) and (b)). A high density of short SFs (few examples are marked by dashed circles) is visible. The inset in (a) shows a magnified view of the SmBCO/LAO interface, where a $b/2$ shift is observed. (c) High-resolution HAADF-STEM image of a Sm_2CuO_4 particle at the film/substrate marked by a dashed red line (for crystal-structure analysis *cf* supplementary information figures S3(c) and (d)). (d) Overlaid power spectra for Sm_2CuO_4 (red) and LAO (blue) from the regions marked with a dashed line in (c).

BHO–SmBCO nanocomposite shows slightly larger values especially for low fields (1 T values: $4.6 \cdot 10^4$ K vs. $5.4 \cdot 10^4$ K), and both samples show roughly a square root dependence in low fields (characteristic for plastic pinning) and a linear dependence at higher fields (characteristic for collective pinning). A linearity analysis between the residual resistance near T_c and U_0 yields an estimate for T_c , which is 93.9 K for both samples within error bars. This value is consistent with two other criteria: maximum slope (93.5 K) and extrapolation of the logarithmic derivative $(d \ln R / dT)^{-1}$ to zero (94.0 K), which is related to the excess conductivity analysis (not followed here), see also supplement. This corresponds to the aforementioned 75% onset- T_c resistivity criterion for B_{c2} .

At higher fields, both samples show a characteristic kink in their transitions (arrow in figure 9). Since this kink is not observed at low fields, inhomogeneities and grain boundary effects can be excluded as explanations. It rather characterizes the beginning of a transition region between the thermally activated flux motion and the fluctuation region near T_c with strong excess conductivity. The transition region itself shows a rather linear behaviour, characteristic for flux flow. This kink behaviour has been observed in different REBCO films, e.g. [66–69], for a theoretical description see e.g. [69, 70].

Figure 11 shows the B – T phase diagram of the BHO–SmBCO nanocomposite for B_{llc} (the one for pristine SmBCO is very similar). $B_{c2}(T)$ was linearly fitted with

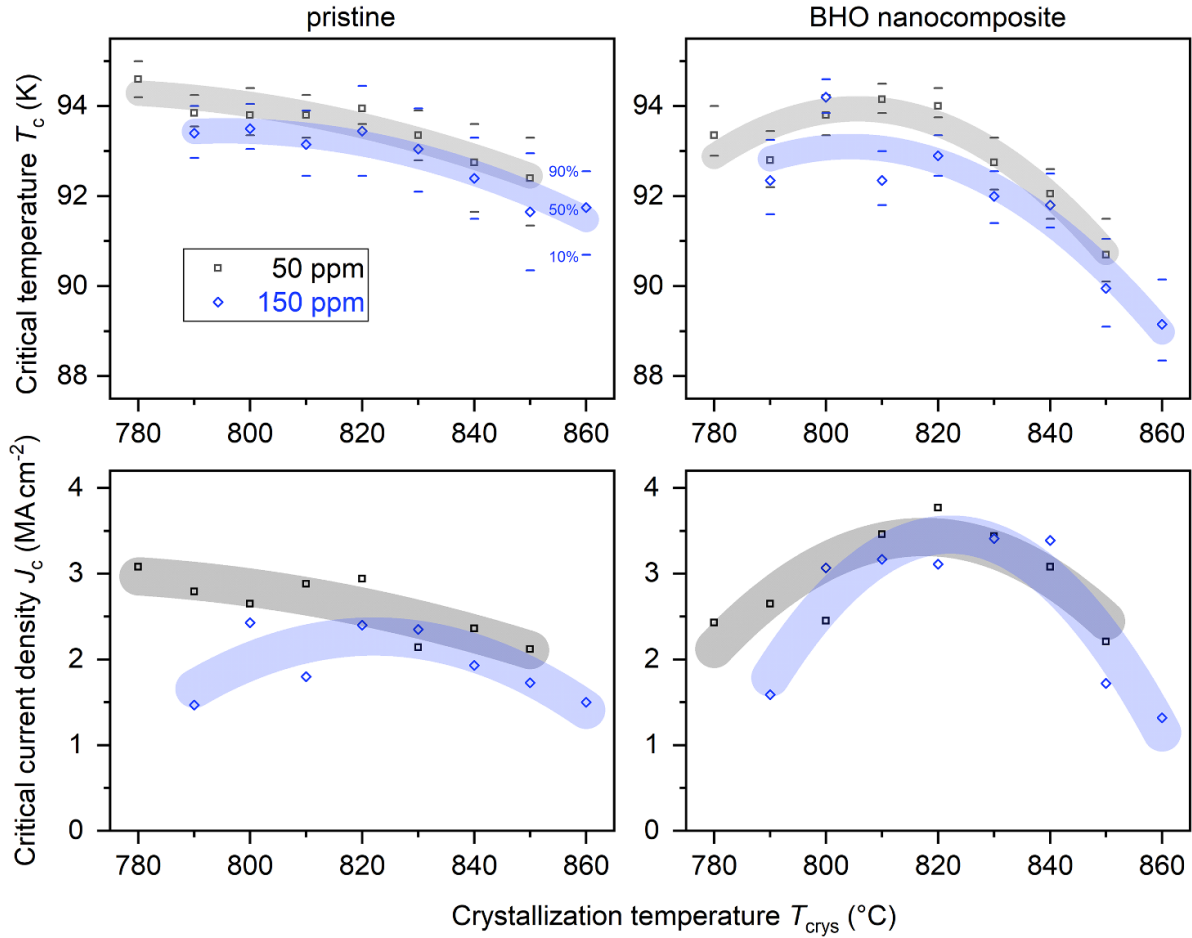


Figure 6. Crystallization temperature dependence of critical temperature T_c and self-field critical current density J_c at 77 K (both measured inductively) for pristine (left) and nanocomposite SmBCO films grown at an oxygen partial pressure of 50 ppm (black) or 150 ppm (blue). The dashes in the upper panels mark the transition width $\Delta T_c = T_{c90} - T_{c10}$ (90% and 10% of transition). The shaded areas are quadratic fits (95% confidence interval) as guide for the eye.

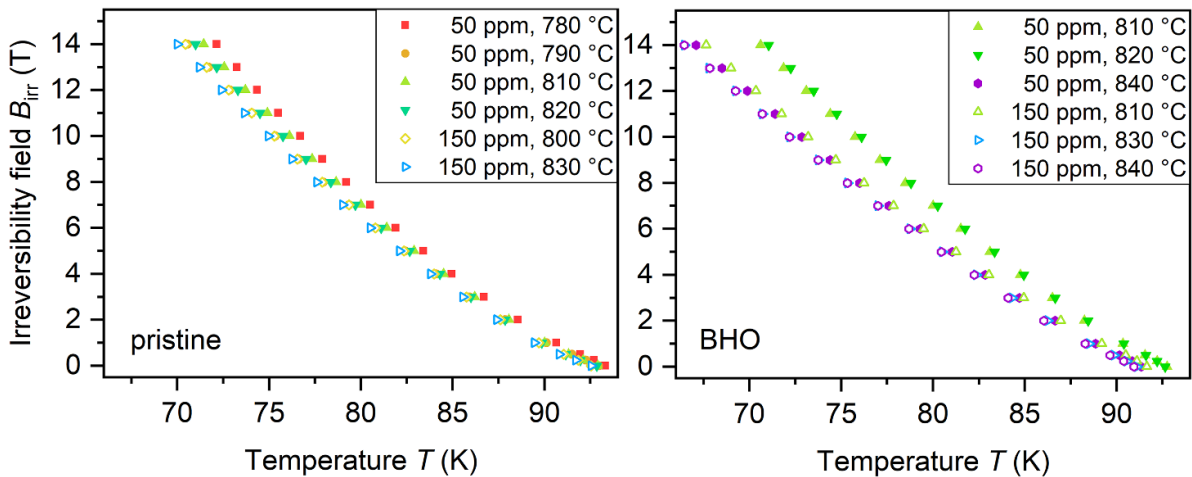


Figure 7. Temperature dependence of the irreversibility field B_{irr} for pristine (left) and BHO nanocomposite SmBCO films (right) prepared at different crystallization temperatures and an oxygen partial pressure of 50 ppm (full symbols) and 150 ppm (open symbols).

slope $dB_{c2}/dT|_{T_c} = 1.50 \pm 0.02$ and $T_c = 93.9 \pm 0.1$ K. The werthamer-helfand-hohenberg (WHH) estimate [71] of the zero-temperature orbital upper critical field $B_{c2}(0) = 0.69dB_{c2}/dT|_{T_c}T_c$ yields 97 ± 1.5 T and consequently

a coherence length $\xi_{ab}(0) = 1.84 \pm 0.01$ nm. The irreversibility field could well be fitted with a power law $B_{irr}(T) = B_{irr}(0)(1 T/T_0)^q$, with $B_{irr}(0) = 76 \pm 1.6$ T, $T_0 = 93.1 \pm 0.2$ K, and an exponent $q = 1.32 \pm 0.02$. The 95% confidence intervals for

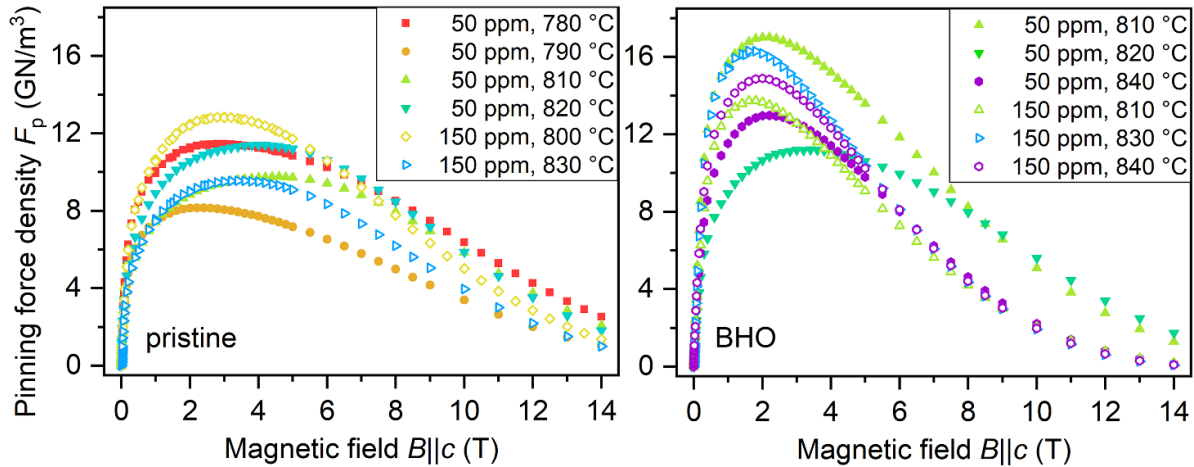


Figure 8. Magnetic field dependence of the pinning force density F_p at 65 K for several pristine (left) and BHO nanocomposite SmBCO films (right) prepared at different crystallization temperatures and an oxygen partial pressure of 50 ppm (full symbols) and 150 ppm (open symbols).

Table 1. Comparison of achievable increase in maximum pinning force density F_{pmax} by randomly oriented $BaMO_3$ (M : Hf or Zr) nanoparticles in MOD-grown REBCO films at 65 or 77 K.

RE	Additive	Content (mol%)	$F_{pmax}^{BMO} / F_{pmax}^{prist}$	T (K)	References
Sm	BHO	12	1.5	77	This work
Sm	BHO	12	1.3	65	This work
Gd	BHO	12	1.4	77	[30]
Gd	BHO	12	3.8	77	[33]
Gd	BHO	12	4.5	65	[33]
Gd _{0.5} Y _{0.5}	BZO	25 ^a	2.5	65	[34]
Gd _{0.5} Y _{0.5}	BHO	25 ^a	6.5	65	[34]
Y	BHO	16 ^b	1.5	77	[63]
Y	BHO	12	3.3	77	[30]
Y	BZO	10	3.0	77	[64]
Y	BZO	10	7.0	77	[37]
Y	BZO	10	9.8	77	[65]
Y	BZO	10	10.4	65	[38]

^a Calculated from 12 vol% in [34].

^b Calculated from 1.5 at% in [63].

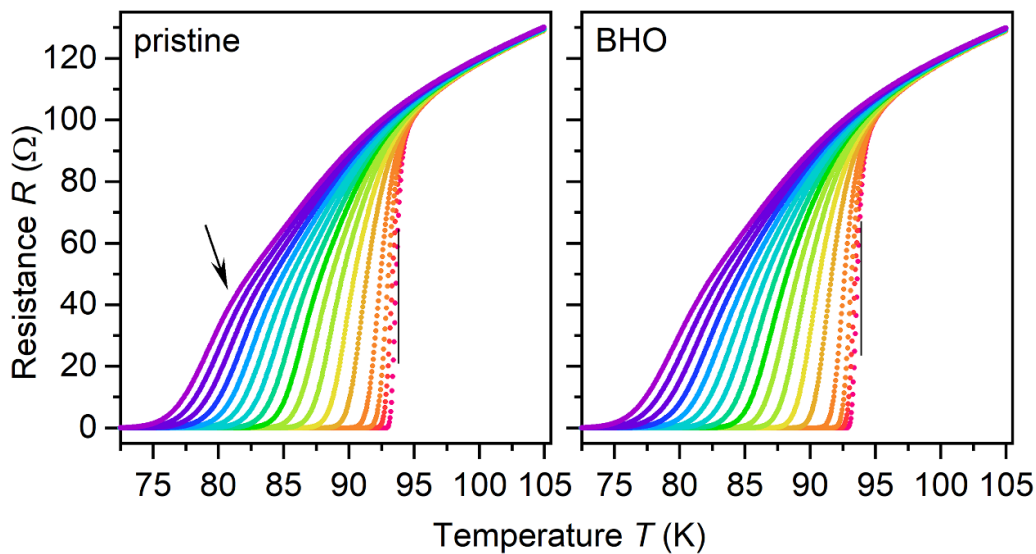


Figure 9. Temperature dependence of the resistance in various magnetic fields $B||c$ between 0 and 14 T (step size 1 T, additionally 0.5 and 0.25 T) for a pristine (left) and a BHO nanocomposite SmBCO film (right). Arrow: kink due to a transition to the flux flow region, lines: T_c of 93.9 K.

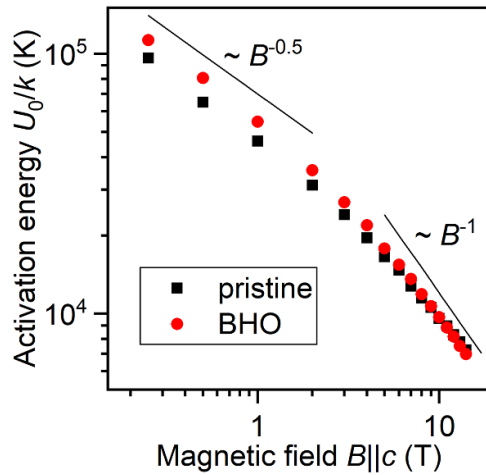


Figure 10. Field dependence of the flux motion thermal activation energy U_0 . The BHO–SmBCO nanocomposite (red) shows slightly larger values than the pristine sample at low fields. The theoretical dependencies for plastic pinning ($U_0 \sim B^{-0.5}$) and collective pinning ($U_0 \sim B^{-1}$) are shown as guide.

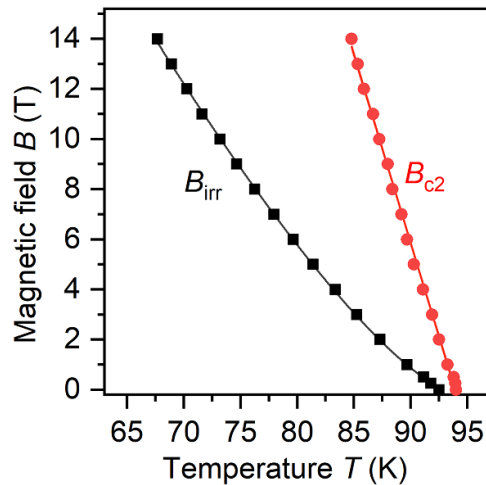


Figure 11. B – T phase diagram for $B_{||c}$ of a BHO–SmBCO nanocomposite film showing the irreversibility line $B_{irr}(T)$ and the upper critical field $B_{c2}(T)$. The lines are power law and linear fits, respectively, see text for details.

both fits are roughly the line thickness in figure 11. Within the error bars, q is $4/3$, which is characteristic for a glass–liquid transition. This transition, however, could not be determined unambiguously from the present data set. $B_{irr}(0)$ being much smaller than $B_{c2}(0)$ can have two origins: either B_{c2} is not orbitally limited at low T and/or $B_{irr}(T)$ shows an upturn at low T due to a possible extra pinning component. High-field measurements may clarify this.

4.3. Field and angular dependence of J_c

The addition of BHO nanoparticles to the SmBCO films enhances the pinning force densities and hence the critical current densities mainly at low fields with a crossover at low temperatures around 10 T, figure 12. The self-field critical current

Table 2. Exponents α in the $J_c(B)$ power law region.

T (K)	Pristine	BHO
30	0.55	0.68
50	0.62	0.72
65	0.69	0.74
77	0.84	0.92

densities of both films are very similar; only at 77 K does the BHO sample show slightly lower values. Whereas there is a clear power law region $J_c(B) \sim B^{-\alpha}$ visible for the pristine sample, it is not as clear for the BHO nanocomposite, especially at elevated temperatures. Nevertheless, when analysed in the same field range of highest linearity for a certain temperature, it is obvious that α increases with increasing temperature for both films, and $\alpha_{pristine} < \alpha_{BHO}$ for all temperatures, table 2. The latter is explained by an increase of the accommodation field (i.e. the length of the constant J_c plateau at lowest fields) and a decrease of the irreversibility field (especially at low T) by BHO addition.

The medium-field range of increased J_c and F_p by BHO addition is also clearly distinguishable by an increase in N value, though in somewhat smaller ranges at high temperatures, figure 12. The N value, i.e. the exponent of power law $E(J)$ curves $E \sim J^N$, is in first approximation related to the flux creep rate $S \cong \frac{1}{N-1}$. In lowest fields however, the BHO nanocomposites show somewhat lower N values for $T \geq 50$ K, which may be due to an increased inhomogeneity, i.e. in local J_c variance. For medium fields and temperatures ($T \leq 65$ K), the N value seems not to depend on temperature for both samples. For the lower temperatures, and especially for the nanocomposites, a region of nearly field-independent N value (i.e. creep rate) is observed before the N value tends towards 1 for fields going to B_{irr} .

The pinning force density curves $F_p(B)$ clearly show the above-mentioned crossover at around 10 T (at low T). This indicates a reduction in the irreversibility field by BHO addition and an already high pinning efficiency of the pristine films' microstructure. The pinning force curves of the pristine samples can be approximated by a Dew-Hughes function $F_p(B) \sim B^p(1 - B/B_{irr})^q$ with $(p, q) \sim (0.5, 2)$, which suggests surface pinning or random pinning at sufficiently small defects. The parameter q is actually often slightly larger than 2 (close to 3) due to the stronger flux creep effects near B_{irr} . The F_p curves of the BHO nanocomposites, more than for the pristine films, however cannot be described well by a single Dew-Hughes function with physically reasonable combinations of B_{irr} and q . This is due to an extra low-field component of the extended BHO nanoparticles at around 1 T. A similar behaviour has been observed recently on all-CSD-grown YBCO nanocomposite coated conductors with BZO and BHO nanoparticles [72].

The angular dependence of the critical current density and of the corresponding N value, figure 13, with respect to field orientation in fields up to 14 T of the pristine and the BHO nanocomposite film are very similar. A strong ab -peak in $J_c(\theta)$ due to electronic anisotropy (random pinning and intrinsic

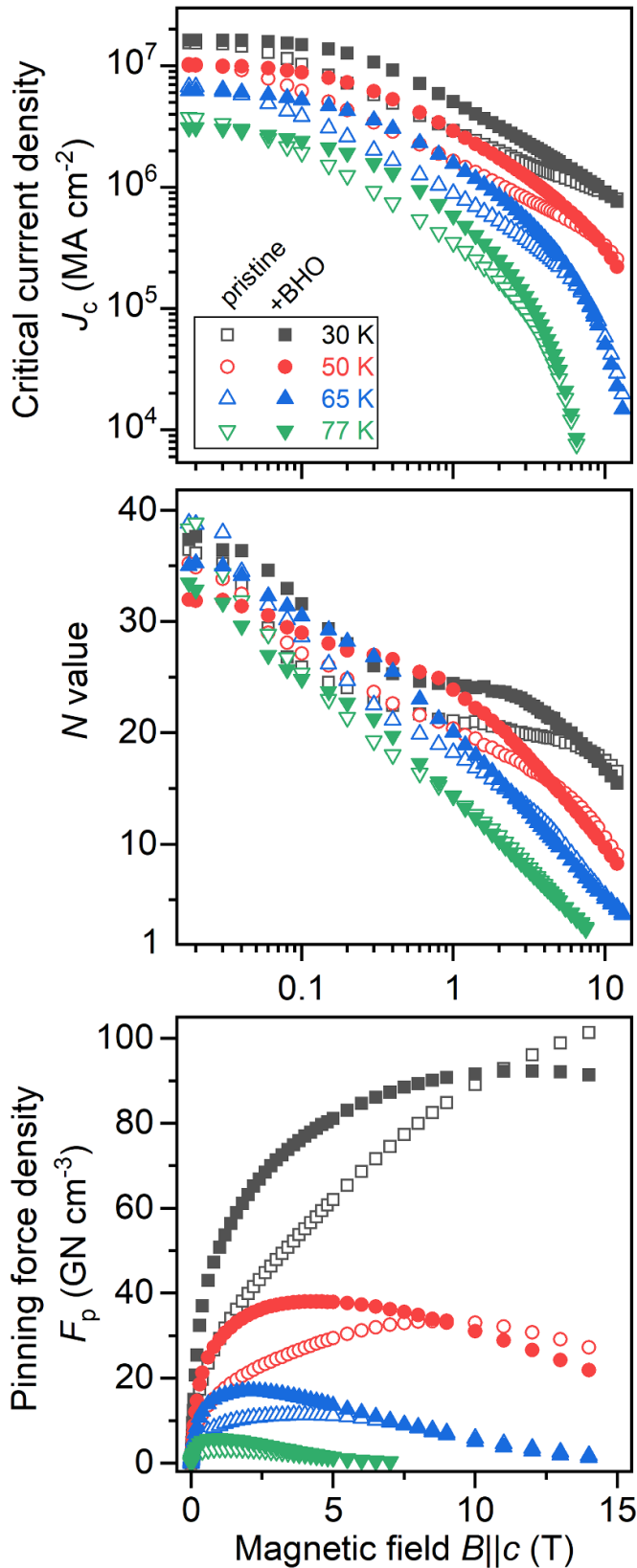


Figure 12. Magnetic field dependence of J_c , N value, and F_p at several temperatures for $B||c$. Comparison between a pristine (open symbols) and a BHO-nanocomposite film (closed symbols).

pinning at low temperatures) as well as correlated pinning at planar defects (SFs) is clearly visible. Close to the irreversibility line, i.e. at sufficiently high fields and temperatures, a small c -axis peak is appearing; most likely due to extended planar (anti-phase boundaries, twin boundaries, domain boundaries) or linear defects (dislocation networks) parallel to the c -axis. At medium fields and low temperatures—more for the pristine sample— $J_c(\theta)$ shows a dip near $B||c$. This also can be attributed to planar defects, namely vortex channelling effects at twin boundaries [73]. The BHO particles hence reduce this channelling effect either directly by increased pinning or indirectly by leading to a reduced density of extended twin boundaries. By BHO nanoparticles being effective in a wide angular range around $B||c$, cf figure 12, the J_c anisotropy is decreased by BHO incorporation at all temperatures. Figure 14 compares the J_c anisotropy at 24 T for several temperatures between the pristine and the BHO-nanocomposite film. Above 30 K, both films behave surprisingly similar.

Further information about the present pinning species and mechanisms are gained by the study of the N value anisotropy. First of all, it usually enhances features due to its averaging effect, see e.g. the extra pinning component of additional medium angle peaks in $N(\theta)$ (e.g. peak around 135° at 65 K, 3 T), which are not or barely visible in $J_c(\theta)$ and due to the sparsely distributed nanoparticles larger than ξ . In these regions, N scales well with J_c , since both depend on the pinning potential U_0 , and the pinning behaviour is dominated by the elastic properties of the flux lines. In contrast, at sufficiently low temperatures, $N(\theta)$ shows a strong dip whereas $J_c(\theta)$ has a maximum. Here, N and J_c are anticorrelated and the creep rate is not determined by the pinning potential anymore but influenced by a second creep mechanism. In this region, the flux lines build staircase patterns of segments strongly pinned (trapped) within the ab -planes/ ab -planar defects and weakly pinned segments with oblique angle to the ab -planes. The easy movement of the weakly pinned segments leads to a net hopping behaviour of the trapped segments from one planar pinning centre to the next, increasing the creep rate and hence decreasing the N value. At the lowest temperatures (see 30 K) and even smaller angles between B and the ab -planes, the whole flux lines will be trapped in the planar pinning centres, which hinders the flux lines from the net hopping movement, thus decreasing the creep rate, and hence increasing the N value. As is apparent in figure 13, especially at low T , the addition of BHO nanoparticles increases the widths of these regions. This is due to the shortening of the trapped segments due to the direct interaction with the nanoparticles and/or a shortening of the planar defects. Interestingly, the trapping angle seems rather field-independent for the pristine sample at medium temperatures, while a $B^{-3/4}$ dependence would be expected by theory. This had been observed also for NdFeAs(O,F) films and was explained by the vicinity of the 2D–3D transition [74]. Finally, we would like to point the attention to the slight c -axis peak in $N(\theta)$ at 14 and 24 T, 30 K for the pristine sample, indicating a

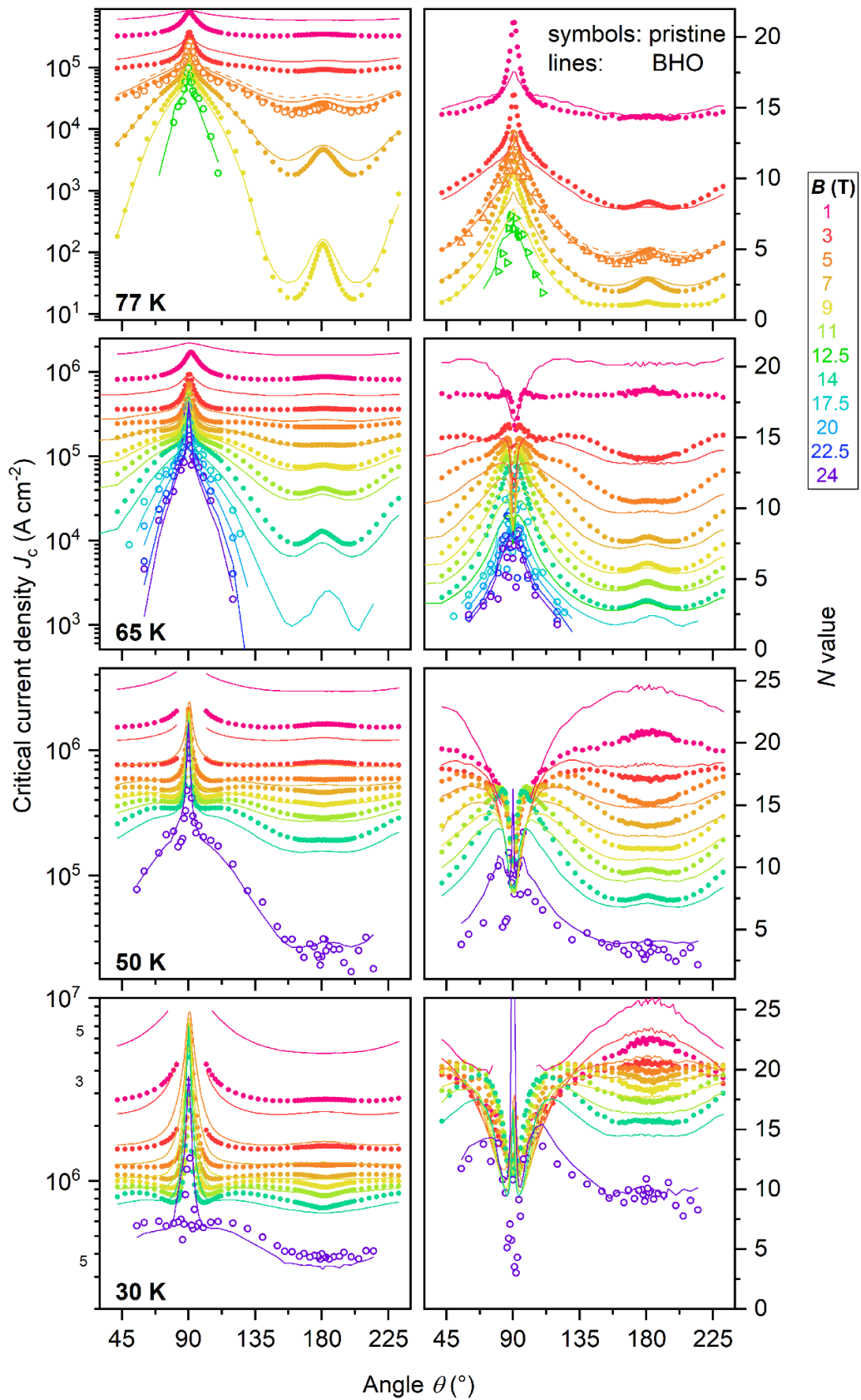


Figure 13. Anisotropy of the critical current density J_c (left panels) and of the N value (right panels) of a pristine (symbols) and a BHO nanocomposite SmBCO film (lines) at several temperatures and applied magnetic fields. The angle θ is measured between the magnetic field and the crystallographic c -axis, i.e. film normal. The open symbols and corresponding lines (dashed at 5 T, 77 K) were measured at IMR Tohoku University.

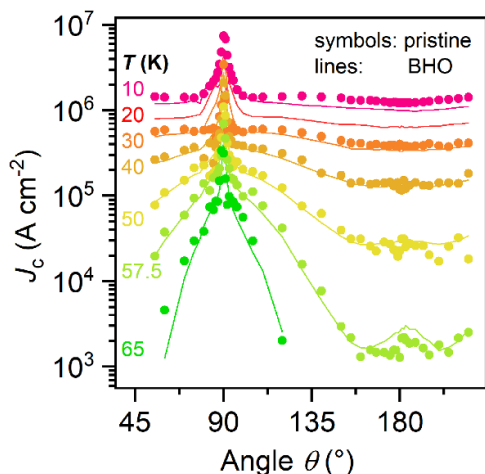


Figure 14. Angular dependence of J_c of a pristine (symbols) and a BHO nanocomposite SmBCO film (lines) at 24 T and several temperatures. 20 K data of pristine sample not available.

decreased creep rate at minimum J_c . Most likely, the extra pinning contribution is hidden by the strong intermediate peaks in $J_c(\theta)$ and gets only apparent in the creep rate.

5. Conclusion

The growth of $\text{SmBa}_2\text{Cu}_3\text{O}_{7-\delta}$ films with and without BHO nanoparticles by CSD was investigated and optimized regarding the crystallization step. Crystallization temperatures around 810 °C and a low oxygen partial pressure of 50 ppm yield the best results regarding T_c and self-field J_c . With XRD as well as a detailed TEM study, a complex microstructure with several foreign phases, such as CuO, Sm_2CuO_4 , and $\text{Sm}_2\text{Cu}_2\text{O}_5$, was detected. Due to the release of trapped fluorine (either within the crystal structure or as OF phase in voids), the samples undergo an aging process with distinct changes in microstructure and—at least initially—an improvement in T_c and J_c . The transport properties, measured in fields up to 24 T revealed a positive effect of the BHO nanoparticles only in small fields up to ~ 10 T, which is due to the already rich pinning landscape in the pristine films. The exact microstructural reasons for the aging process as well as an optimization of nanoparticle insertion for pinning improvement may be tasks of future studies.

Data availability statement

TEM images and data analysis for figures 3 and 4 are available at Zenodo [75].

The data that support the findings of this study are available upon reasonable request from the authors.

Acknowledgments

This work was supported by Japan–Germany Research Cooperative Program between JSPS and DAAD, Grant Nos.

JPJSBP120203506 and 57523294. A part of this work was performed at High Field Laboratory for Superconducting Materials, Institute for Materials Research, Tohoku University (Project Number 19H0507). We thank Kai Walter (ITEP-KIT) for further information regarding XRD.

ORCID iDs

Jens Hänisch <https://orcid.org/0000-0003-2757-236X>
 Kazumasa Iida <https://orcid.org/0000-0003-1038-9630>
 Pablo Cayado <https://orcid.org/0000-0003-3703-6122>
 Manuela Erbe <https://orcid.org/0000-0001-9698-1509>
 Lukas Grünewald <https://orcid.org/0000-0002-5898-0713>
 Takafumi Hatano <https://orcid.org/0000-0002-6509-5835>
 Tatsunori Okada <https://orcid.org/0000-0002-6513-3758>
 Dagmar Gerthsen <https://orcid.org/0000-0003-2406-5805>
 Satoshi Awaji <https://orcid.org/0000-0003-2043-1628>
 Bernhard Holzapfel <https://orcid.org/0000-0002-8420-4777>

References

- [1] Obradors X and Puig T 2014 *Supercond. Sci. Technol.* **27** 044003
- [2] MacManus-Driscoll J L and Wimbush S C 2021 *Nat. Rev. Mater.* **6** 587–604
- [3] Yao X, Zeng X H and Xu S 2004 *Physica C* **412-414** 90–93
- [4] Jia Q X, Foltyn S R, Coulter J Y, Smith J F and Maley M P 2002 *J. Mater. Res.* **17** 2599–603
- [5] Xiong J, Qin W, Cui X, Tao B and Li Y 2006 *J. Supercond.* **19** 29–32
- [6] Abrutis A, Bartasyte A, Saltyte Z, Zukova A, Donet S and Weiss F 2004 *Physica C* **415** 21–28
- [7] Wang T, Tu R, Zhang C, Zhang S, Wang K, Goto T and Zhang L 2021 *J. Asian Ceram. Soc.* **9** 197–207
- [8] Nigro A, Grimaldi G, Savo B, Pace S, Boffa M A and Cucolo A M 2004 *Physica C* **401** 277–81
- [9] Lee B S, Chung K C, Lim S M, Kim H J, Youm D and Park C 2004 *Supercond. Sci. Technol.* **17** 580–4
- [10] Tang C Y, Cai Y Q, Li W, Sun L J, Yao X and Jirsa M 2009 *Cryst. Growth Des.* **9** 1339–43
- [11] Wang Z, Wang W T, Yang X F, Wang M J and Zhao Y 2014 *J. Supercond. Nov. Magn.* **27** 1801–6
- [12] Erbe M, Cayado P, Freitag W, Ackermann K, Langer M, Meledin A, Hänisch J and Holzapfel B 2020 *Supercond. Sci. Technol.* **33** 94002
- [13] Li M, Cayado P, Erbe M, Jung A, Hänisch J, Holzapfel B, Liu Z and Cai C 2020 *Coatings* **10** 31
- [14] Zhang H, Zhao Y, Zhang Y, Pan M and Lei M 2015 *Int. J. Mod. Phys. B* **29** 1542040
- [15] Fuger R, Eisterer M, Oh S S and Weber H W 2010 *Physica C* **470** 323–5
- [16] Knibbe R, Strickland N M, Wimbush S C, Puichaud A-H and Long N J 2016 *Supercond. Sci. Technol.* **29** 65006
- [17] Cayado P, Li M, Erbe M, Liu Z, Cai C, Hänisch J and Holzapfel B 2020 *R. Soc. Open Sci.* **7** 201257
- [18] Talantsev E F, Strickland N M, Wimbush S C, Storey J G, Tallon J L and Long N J 2014 *Appl. Phys. Lett.* **104** 242601
- [19] Ozaki T, Yoshida Y, Miura M, Ichino Y, Takai Y, Matsumoto K, Ichinose A, Horii S and Mukaida M 2007 *IEEE Trans. Appl. Supercond.* **17** 3270–3
- [20] Yoshida Y, Matsumoto K, Miura M, Ichino Y, Takai Y, Ichinose A, Horii S and Mukaida M 2005 *Jpn. J. Appl. Phys.* **44** L546–L548

- [21] Choi W J, Ahmad D, Seo Y I, Ko R K and Kwon Y S 2020 *Sci. Rep.* **10** 2017
- [22] Jha A K and Matsumoto K 2019 *Front. Phys.* **7** 1–21
- [23] Matsumoto K and Mele P 2010 *Supercond. Sci. Technol.* **23** 14001
- [24] Obradors X, Puig T, Palau A, Pomar A, Sandiumenge F, Mele P and Matsumoto K 2011 Nanostructured superconductors with efficient vortex pinning *Comprehensive Nanoscience and Technology* ed D L Andrews (Amsterdam: Elsevier) ch 3.10, pp 303–49
- [25] Sun M J, Liu W Q, Zhou H B, He K, Yu M, Liu Z Y, Lu Y M, Cai C B and Chen S G 2018 *J. Supercond. Nov. Magn.* **31** 3679–83
- [26] Yoshida Y, Miura S, Tsuchiya Y, Ichino Y, Awaji S, Matsumoto K and Ichinose A 2017 *Supercond. Sci. Technol.* **30** 104002
- [27] Wu J and Shi J 2017 *Supercond. Sci. Technol.* **30** 103002
- [28] Tsuchiya Y, Awaji S, Watanabe K, Miura S, Ichino Y, Yoshida Y and Matsumoto K 2016 *J. Appl. Phys.* **120** 103902
- [29] Tsuruta A, Yoshida Y, Ichino Y, Ichinose A, Matsumoto K and Awaji S 2014 *J. Phys.: Conf. Ser.* **507** 22043
- [30] Erbe M et al 2015 *Supercond. Sci. Technol.* **28** 114002
- [31] Bretos I, Schneller T, Falter M, Bäcker M, Hollmann E, Wördenweber R, Molina-Luna L, van Tendeloo G and Eibl O 2015 *J. Mater. Chem. C* **3** 3971–9
- [32] Lei L, Liu L, Wang X, Wang S, Jia J, Zhao G, Wu C, Jin L, Li C and Zhang P 2016 *J. Mater. Chem. C* **4** 1392–7
- [33] Cayado P, Erbe M, Kauffmann-Weiss S, Bühler C, Jung A, Hänisch J and Holzapfel B 2017 *Supercond. Sci. Technol.* **30** 094007
- [34] Miura M et al 2017 *NPG Asia Mater.* **9** e447–e447
- [35] Matsutani F, Takahashi Y, Kiuchi M, Otabe E S, Matsushita T, Miura M, Izumi T and Shiohara Y 2010 *Physica C* **470** 1411–4
- [36] Erbe M, Hänisch J, Freudenberg T, Kirchner A, Mönch I, Kaskel S, Schultz L and Holzapfel B 2014 *J. Mater. Chem. A* **2** 4932
- [37] Llordés A et al 2012 *Nat. Mater.* **11** 329–36
- [38] Gutiérrez J et al 2007 *Nat. Mater.* **6** 367–73
- [39] Langford R M and Clinton C 2004 *Micron* **35** 607–11
- [40] Schlossmacher P, Klenov D O, Freitag B and von Harrach H S 2010 *Micros. Today* **18** 14–20
- [41] Jolliffe I T and Cadima J 2016 *Phil. Trans. A* **374** 20150202
- [42] Peña F de la et al 2017 *Microsc. Microanal.* **23** 214–5
- [43] Peña F de la et al 2021 hyperspy/hyperspy: release v1.6.4 (Zenodo) (<https://doi.org/10.5281/zenodo.5082777>)
- [44] Mitani A et al 2008 *Physica C* **468** 1546–9
- [45] Tkachenko N L, Garashina L S, Izotova O E, Aleksandrov V B and Sobolev B P 1973 *J. Solid State Chem.* **8** 213–8
- [46] Gàzquez J, Sandiumenge F, Coll M, Pomar A, Mestres N, Puig T, Obradors X, Kihn Y, Casanove M J and Ballesteros C 2006 *Chem. Mater.* **18** 6211–9
- [47] Lee K H, Park S S, Jo C G, Lee W R, Lee H M and Choi U-S 1996 *Solid State Commun.* **100** 365–70
- [48] Fedorenko V V et al 1994 *Physica C* **221** 71–75
- [49] Li Z, Coll M, Mundet B, Palau A, Puig T and Obradors X 2019 *J. Mater. Chem. C* **7** 4748–59
- [50] Smith J D, Huh J, Shelton A, Reidy R F and Young M L 2021 *Microsc. Microanal.* **27** 1338–55
- [51] Wong-Ng W, Paretzkin B and Fuller E R 1990 *J. Solid State Chem.* **85** 117–32
- [52] Farbod M and Rafati Z 2019 *Phase Trans.* **92** 773–81
- [53] Kol'tsova T N 2004 *Inorg. Mater.* **40** 656–60
- [54] Park I, Oh W J, Lee J H, Moon S H and Yoo S I 2018 *Prog. Supercond. Cryog.* **20** 46–49
- [55] Wang T, Zhang S, Yang M, Tu R, Goto T and Zhang L 2017 *Ceram. Int.* **43** S488–92
- [56] Pavan Kumar Naik S, Missak Swarup Raju P, Rajasekharan T and Seshubai V 2014 *J. Supercond. Nov. Magn.* **27** 1211–5
- [57] Zhu Y, Tsai C-F and Wang H 2013 *Supercond. Sci. Technol.* **26** 25009
- [58] Zandbergen H W 1992 *Physica C* **193** 371–84
- [59] Zakharov N D, Kästner G, Hesse D and Lorenz M 1996 *Appl. Phys. Lett.* **69** 1151–3
- [60] Yu Z, Muller D A and Silcox J 2004 *J. Appl. Phys.* **95** 3362–71
- [61] Uzumaki T, Kamehara N and Niwa K 1991 *Jpn. J. Appl. Phys.* **30** L981–4
- [62] Cayado P, Rijckaert H, Erbe M, Langer M, Jung A, Hänisch J and Holzapfel B 2020 *Nanomaterials* **10** 21
- [63] Engel S, Thersleff T, Hühne R, Schultz L and Holzapfel B 2007 *Appl. Phys. Lett.* **90** 102505
- [64] de Keukeleere K et al 2016 *Adv. Electron. Mater.* **2** 1600161
- [65] Petrisor T, Mos R B, Nasui M, Gabor M S, Augieri A, Celentano G, de Felicis D, Bemporad E and Ciontea L 2014 *J. Supercond. Nov. Magn.* **27** 2493–500
- [66] Stangl A, Palau A, Deutscher G, Obradors X and Puig T 2021 *Sci. Rep.* **11** 8176
- [67] Huhtinen H, Irjala M and Paturi P 2012 *Phys. Proc.* **36** 503–7
- [68] Romanov A, Krkotić P, Telles G, O'Callaghan J, Pont M, Perez F, Granados X, Calatroni S, Puig T and Gutierrez J 2020 *Sci. Rep.* **10** 12325
- [69] Rey R I, Carballeira C, Doval J M, Mosqueira J, Ramallo M V, Ramos-Álvarez A, Sónora D, Veira J A, Verde J C and Vidal F 2019 *Supercond. Sci. Technol.* **32** 45009
- [70] Ikeda R, Ohmi T and Tsuneto T 1991 *J. Phys. Soc. Japan* **60** 1051–69
- [71] Werthamer N R, Helfand E and Hohenberg P C 1966 *Phys. Rev.* **147** 295–302
- [72] Díez-Sierra J et al 2021 *Supercond. Sci. Technol.* **34** 114001
- [73] Rouco V, Palau A, Guzman R, Gazquez J, Coll M, Obradors X and Puig T 2014 *Supercond. Sci. Technol.* **27** 125009
- [74] Tarantini C et al 2016 *Sci. Rep.* **6** 36047
- [75] Hänisch J, Iida K, Cayado P, Erbe M, Grünwald L, Hatano T, Okada T, Gerthsen D, Awaji S and Holzapfel B 2022 Supplementary information for “microstructure and pinning properties of CSD-grown $\text{SmBa}_2\text{Cu}_3\text{O}_{7-\delta}$ films with and without BaHfO_3 nanoparticles” (<https://doi.org/10.5281/ZENODO.6350486>)